

Self-calibration for lab- μ CT using space-time regularized projection-based DVC and model reduction

C Jailin¹, A Buljac^{1,2}, A Bouterf¹, M Poncelet¹, F Hild¹ and S Roux¹

¹ LMT (ENS Paris-Saclay/CNRS/Univ. Paris-Saclay) 61 avenue du Président Wilson, F-94235 Cachan (FRANCE)

² MINES ParisTech, PSL Research University, Centre des Matériaux, CNRS UMR 7633, BP 87, 91003 Evry, France

E-mail: clement.jailin@ens-paris-saclay.fr

Abstract. An online calibration procedure for X-ray lab-CT is developed using projection-based digital volume correlation. An initial reconstruction of the sample is positioned in the 3D space for every angle so that its projection matches the initial one. This procedure allows a space-time displacement field to be estimated for the scanned sample, which is regularized with i) rigid body motions in space and ii) modal time shape functions computed using model reduction techniques (*i.e.*, proper generalized decomposition). The result is an accurate identification of the position of the sample adapted for each angle, which may deviate from the desired perfect rotation required for standard reconstructions. An application of this procedure to a 4D *in situ* mechanical test is shown. The proposed correction leads to a much improved tomographic reconstruction quality.

Keywords: X-ray Computed Tomography; Online calibration; Artifact correction; Digital Volume Correlation; Proper Generalized Decomposition (PGD)

Submitted to: *Meas. Sci. Technol.*

1. Introduction

Micro-Computed Tomography (μ -CT) is widely used for non-destructive imaging [1, 2]. It consists in reconstructing full 3D volumes of a sample from sets of radiographs and a reconstruction algorithm [3]. From the first developments with parallel X-ray beams in synchrotron facilities, it is now an accessible equipment in laboratories. Recent developments allow for imaging at high spatial and temporal resolutions [4, 5].

To deal with the reconstruction procedure (*i.e.*, an inverse Radon transform), different algorithms exist such as filtered back projection (FBP), its (Feldkamp-Davis-Kress) extension [6] for cone beam geometries or algebraic methods [3]. All these

reconstruction methods require the geometric parameters of the tomograph (*e.g.*, position and orientation of the source, rotation axis and detector, pixel sizes) to be known. If the geometric parameters are not well calibrated or if they change in time, the reconstruction suffers from artifacts that may create blur or magnification effects. They may forbid the quantitative use of the acquired volumes (*e.g.*, space-time full-field measurements [7]).

Various types of methods exist to estimate the 9 geometric parameters for cone-beam X-ray CT [8]. These methods can be separated into two categories, namely, *offline* and *online* calibration.

Offline procedures are calibrations using a perfectly known pattern with radiopaque markers. Virtual projections of this geometry have to match the acquired projections. In Refs. [9, 10, 11], the known patterns are composed of few steel balls whose orbits are measured during the rotation of the turntable. In Refs. [12, 13, 14, 15], the authors used an iterative procedure to identify geometric parameters from a known complex phantom and a single projection. These offline methods, which are based on a known pattern or phantom, often have to be performed before or after the real test. The parameters are generally identified only once, even for a multi-acquisition test (*e.g.*, a 4D *in situ* mechanical test) in order not to move the sample during repeated scans. The parameters are therefore assumed to be stable in time. However, in some cases, this assumption may be violated and lead to blurred reconstructions. A variety of causes can be listed, such as motions of the sample or the entire set-up due to unsteady thermal expansion [16], creep (*i.e.*, delayed mechanical response [17]) of the sample under load, motion of a mechanical testing machine due to its compliance, accidental hitting, uncompensated backlash).

Online calibration is the measurement of the geometric parameters directly using the projections by exploiting knowledge of the object being imaged. In the spirit of offline procedures, Andò [18] used a known frame attached to the sample to find the geometric parameters of the scan during acquisition. Pannetta *et al* [19] proposed a calibration method based on the minimization of the quadratic difference between projections at a certain angle and the mirror projection at the opposed angle (for parallel beam). Kyriakou *et al* [20] developed an optimization of geometric parameters based on the minimization of the information entropy of the reconstructed volume. With 3D-2D image registration [21, 22], Ouadah *et al* [23] used a pre-scanned 3D image as the reference volume (hence a known very complex pattern). In Ref. [24], a motion tracking system allows for measuring and then compensating the *in situ* motion of the acquired image. A recent publication of Sun *et al* [25] proposed an optimization procedure based on the initial reconstruction of the volume with a first set of geometric parameters. Then the minimization of the “projection residual” fields (*i.e.*, the difference between the projected reconstructed volume and the initial sinogram) with respect to rigid body motions of the volume, provides an estimate of the motion of the scanned sample. This motion is finally used for the correction of projections. For the application aimed by the authors, *i.e.*, patient motion compensation for medical imaging, the

measured displacement field is large (5-20 voxels as an order of magnitude), and cannot be smaller due to several assumptions or approximations (on the sensitivities, on the axial displacement supposed to be null, on filtering).

A robust and accurate method that measures sub-pixel or sub-voxel displacements of patterns between different images is provided via Digital Image Correlation (DIC) in 2D [26] and Digital Volume Correlation in 3D [27, 28]. A recently developed projection-based Digital Volume Correlation (P-DVC) procedure, in the same spirit as 3D-2D image registration, lies in between 2D DIC and 3D DVC as it deals with 3D displacement fields of the reconstructed reference sample with respect to deformed radiographs with the minimization of a set of 2D error maps. This method was initially developed for the measurement of uniform displacement fields during different steps of a mechanical test [29], with possible cracks [30, 31] and finally for identification purposes in a lab-tomograph [32]. This procedure leads to huge savings in acquisition time. However, as such, P-DVC uses a reconstructed 3D image to evaluate its motion, and is not designed to identify geometrical reconstruction parameters.

In this paper, an online two-step iterative procedure is proposed. First, the rotation axis is identified in the same spirit as Ref. [25], from a pattern that is the loaded sample itself, reconstructed from its projections hence without a perfectly known geometry. Thanks to P-DVC, the sample is repositioned in the laboratory frame so that its projection matches the corresponding acquired projections for every angle. The result is an identification of the sample position at each instant (*i.e.*, projection angle) with a sub-voxel uncertainty and thus projections can be corrected to coincide with nominal geometrical parameters, and allow for reconstructing a new volume and iterate if needed. A major advantage of this procedure is that an imperfect kinematics for the acquisition, such as a precessing rotation axis, can be accounted for, thereby enhancing the reconstruction quality without any additional demand on the acquisition protocol.

The displacement field is decomposed over a basis of separated functions, namely, spatial modes (here chosen to be rigid body motions) and time (or projection angle) modes. Even when restricted over few spatial modes, a large temporal flexibility leads to a poorly conditioned system. Two routes for dealing with such issues are explored. Either few temporal modes are introduced (with the difficulty of choosing a suited temporal basis), or a model reduction technique is used. The spirit of the latter, which is inspired from the Proper Generalized Decomposition (PGD) technique, consists in a progressive enrichment of the space-time modes for displacement corrections. Based on the minimization of the projection residual, a greedy approach extracts one mode per iteration. This model reduction technique reveals very instrumental to determine the displacement modes.

The method based on 4D P-DVC is introduced in Section 2. In Section 3, the application to an *in situ* mechanical test with a cone-beam geometry is performed. The rotation axis is determined with a single iteration of the procedure and the correction of the axis shows significant improvement of the reconstructed volumes.

2. Method

2.1. General principle

In the following, raw radiographs acquired by the CT-scanner are first normalized by their flat fields (*i.e.*, radiographs acquired with the same conditions as the actual scan but without the specimen) and their logarithm computed (*i.e.*, Beer Lambert law) to produce “projections” that constitute the sinogram. It is from such preprocessed data, which will be referred to as “projections,” that reconstructions are performed using the Filtered Back Projection (FBP) algorithm (or suited extensions for cone-beam geometries).

Starting with an initial reconstructed 3D image, hereafter also called “volume”, it is positioned in the 3D space for every projection angle and its projection is computed so that it matches at best the corresponding projection. This difference between initial projection and projected volume is called projection *residual* field. Let us note that these residuals can be interpreted as the sum of four contributions due to:

- (i) acquisition noise and artifacts (*e.g.*, beam hardening, phase contrast, approximations during reconstruction and projection);
- (ii) approximate (or erroneous) geometric parameters of the tomograph in the reconstruction and projection procedure;
- (iii) rigid body motions of the scanned sample during acquisition (*i.e.*, deformation of the testing machine or turntable, uncompensated backlash);
- (iv) deformations of the sample itself (*e.g.*, thermal effects, relaxation). This latter effect is assumed to be null (or extremely small) in the examined case.

2.2. Projection-based digital volume correlation

The proposed method for the identification of the displacement field based on radiographs is Projection-based Digital Volume Correlation (P-DVC) [29]. The first step of the procedure is the acquisition and reconstruction of a reference volume, $f(\mathbf{x})$, from a complete set of N_θ projections $s(\mathbf{r}, \theta)$ and an initial choice of geometric parameters. In the present notations, \mathbf{x} is a 3D vector in the sample frame, \mathbf{r} is a 2D vector denoting positions in the detector frame, and θ the rotation angle. The idea is to estimate the 4D displacement field $\mathbf{u}(\mathbf{x}, \theta)$ so that each projection of the displaced volume $f(\mathbf{x} - \mathbf{u}(\mathbf{x}, \theta_k))$ matches the initial projection, $s(\mathbf{r}, \theta_k)$. After updating the reconstruction, from the corrected displacement, the procedure is iterated until corrections of the geometrical parameters are less than a predetermined threshold.

In the same spirit as global DVC [33], the displacement field is obtained from the minimization of the quadratic difference, $\chi_{\mathbf{u}}^2$, between the (re-)projected 3D image corrected by the displacement field $\Pi_k[f(\mathbf{x} - \mathbf{u}(\mathbf{x}, \theta_k))]$ and the initial sinogram for every

angle $s(\mathbf{r}, \theta_k)$, with Π_k being the conical projection operator along the θ_k direction

$$\chi_u^2 = \frac{1}{N_\theta |\Xi| \gamma_s^2} \sum_{k,r} (\Pi_k[f(\mathbf{x} - \mathbf{u}(\mathbf{x}, \theta_k))] - s(\mathbf{r}, \theta_k))^2 \quad (1)$$

where the double sum over (k, \mathbf{r}) stands for the discrete integration over all pixels $\mathbf{r} \in \Xi$ of the detector (or its utilized part, which will be referred to as region of interest or ROI) and all N_θ projection angles θ_k . γ_s^2 denotes the variance of the sinogram noise, and $|\Xi|$ the area (number of pixels) of Ξ . The normalizing parameters of Equation 1 are chosen in such a way that when the residuals $\rho = \Pi_k[f(\mathbf{x} - \mathbf{u}(\mathbf{x}, \theta_k))] - s(\mathbf{r}, \theta_k)$ are only associated with acquisition noise, $\chi_u = 1$. Any deviation from 1 (*i.e.*, $\chi_u > 1$ is an indication of model error (*i.e.*, the chosen kinematic basis is not fully consistent with the studied experiment).

When small displacement levels are assumed compared to the correlation length of the imaged microstructure, a small perturbation expansion is written about the current estimate \tilde{u} of the displacement field, with $\nabla f(\mathbf{x})$ the gradient of the 3D image

$$\chi_u^2 \approx \frac{1}{N_\theta |\Xi| \gamma_s^2} \sum_{k,r} (\Pi_k[f(\mathbf{x}) - \nabla f(\mathbf{x} - \tilde{u}(\mathbf{x}, \theta_k)) \cdot \delta \mathbf{u}(\mathbf{x}, \theta_k)] - s(\mathbf{r}, \theta_k))^2 \quad (2)$$

so that the minimization operates on a quadratic function of the unknowns, thereby leading to easily accessible search directions. It is noteworthy that after each evaluation of the displacement corrections $\delta \mathbf{u}$, a correction of the volume is performed so that Equation 1 is used without approximation.

2.3. 4D Regularization

Different regularization procedures of the displacement field have been introduced in the literature for global DIC methods where the kinematics is expressed on a finite element mesh. Spatially, a local mechanical elastic constraint, in 2D [34, 35] or 3D [36, 37], strong regularizations or integrated methods with a reduced basis composed of elementary fields from mechanical computation [38, 7]. These regularizations lead to a drastic reduction in the number of unknowns and enable for seamless experimental/numerical procedures.

The displacement field is expressed as a combination of N_m spatial modes $\Phi^i(\mathbf{x})$ that are weighted for each angle by $\alpha^i(\theta_k)$. Such a separated expression is standard practice and as such bears no consequence, but it will reveal convenient for the following model reduction technique

$$\mathbf{u}(\mathbf{x}, \theta_k) = \sum_{i=1}^{N_m} \alpha^i(\theta_k) \Phi^i(\mathbf{x}). \quad (3)$$

The spatial modes are expressed as a reduced basis composed of the 6 Rigid Body Motions (RBMs) $\psi_j(\mathbf{x})$

$$\mathbf{u}(\mathbf{x}, \theta_k) = \sum_{i=1}^{N_m} \sum_{j=1}^6 \alpha_j^i(\theta_k) \psi_j(\mathbf{x}). \quad (4)$$

The time changes $\alpha_j^i(\theta)$ can similarly be constrained by additional temporal regularizations [39, 40]. This constraint may come from previous knowledge or anticipation of the motions. The N_n temporal modes are expressed as elementary functions σ_n (e.g., Dirac distribution if no regularization (free) is considered, polynomials, sinusoidal functions)

$$\alpha_j^i(\theta_k) = \sum_{n=1}^{N_n} a_{jn}^i \sigma_n(\theta_k) \quad (5)$$

where a_{jn}^i are the amplitudes of elementary basis functions being the product of the N_n temporal and N_m spatial modes. In the treated application, the time basis does not change with mode identification thus does not depend on i , but such cases could be designed. The displacement field is finally written as

$$\mathbf{u}(\mathbf{x}, \theta_k) = \sum_{n=1}^{N_n} \sum_{j=1}^6 a_{jn} \sigma_n(\theta_k) \boldsymbol{\psi}_j(\mathbf{x}). \quad (6)$$

Two methods are proposed to solve the minimization problem, depending on the complexity and number of degrees of freedom:

- A full determination of the displacement field, in Section 2.3.1. This method is the most complete but requires an appropriate prior knowledge of time and space basis functions, which may involve many degrees of freedom, and hence possibly poor conditioning. It is referred to as “full identification” in the following.
- A PGD approach, where additional modes are successively determined as long as the residual level is considered too high to be explained by noise (i.e., $\chi_{\mathbf{u}} > 1$). This method is presented in Section 2.3.2.

2.3.1. Full measurement Because the \mathbf{x} referential frame is linked to the rotating sample, a choice of time functions can, for example, be low order Fourier modes, plus possibly linear motions to account for a slow and steady drift that would break periodicity. The full determination of all space and time amplitudes, a_n^i , (the N_n time modes times the $N_m = 6$ spatial modes) may be accessible; the risk being here that the system become poorly conditioned. The following subsection will describe a method to reduce the number of modes to only those that are needed.

The problem is rewritten as

$$\mathbf{u}(\mathbf{x}, \theta_k) = \sum_{n,j} a_{jn} \sigma_n(\theta_k) \boldsymbol{\psi}_j(\mathbf{x}) \quad (7)$$

so that its minimization is achieved with Newton’s descent method. A single uncoupled system is obtained in terms of the corrections δa_{in}

$$\delta a_{in} = \bar{T}_{injm}^{-1} \bar{\mathbf{t}}_{jm} \quad (8)$$

with

$$\bar{T}_{injm} = \sum_{k,r} \sigma_n(\theta_k) \Pi_k[\boldsymbol{\psi}_i(\mathbf{x}') \cdot \nabla f(\mathbf{x}')] \sigma_m(\theta_k) \Pi_k[\boldsymbol{\psi}_j(\mathbf{x}') \cdot \nabla f(\mathbf{x}')] \quad (9)$$

and

$$\bar{t}_{jm} = \sum_{k,r} (s(\mathbf{r}, \theta_k) - \Pi_k[f(\mathbf{x}')]) \sigma_m(\theta_k) \Pi_k[\boldsymbol{\psi}_j(\mathbf{x}') \cdot \nabla f(\mathbf{x}')] \quad (10)$$

2.3.2. Free modal measurement An integrated approach is proposed along the line of Proper Generalized Decomposition (PGD) techniques [41, 42, 43], which consists in successive enrichments of the displacement field $\mathbf{u}(\mathbf{x}, \theta_k)$ summing an additional contribution at each iteration, each term of the sum being sought *a priori* in a separate representation. PGD-DIC and PGD-DVC [44, 45] with one-dimensional space functions is here extended to 3D space-time (angles) analyses.

In the following progressive PGD procedure, the spatial modes, which are defined as $\Phi^i(\mathbf{x}) = p_j^i \boldsymbol{\psi}_j(\mathbf{x})$, will be identified successively, one per iteration, with a greedy approach [46].

$$\mathbf{u}^l(\mathbf{x}, \theta_k) = \mathbf{u}^{l-1}(\mathbf{x}, \theta_k) + \left(\sum_{n=1}^{N_n} a_n^l \sigma_n(\theta_k) \right) \left(\sum_{j=1}^6 p_j^l \boldsymbol{\psi}_j(\mathbf{x}) \right). \quad (11)$$

Let us note that only the product $a_n^l p_j^l$ matters so that an additional convention (but just 1) such as $\|\mathbf{a}^l\| = 1$ or $\|\mathbf{p}^l\| = 1$, could be freely chosen without consequence.

A fixed point algorithm is used to get the solution. Alternate minimizations of the two unknown vectors \mathbf{a}^l and \mathbf{p}^l are proposed. The minimization of the functional leads to the determination of the unknowns with two coupled equations

$$\mathbf{p}^l = \text{Argmin}_{\mathbf{p}^l} (\chi_u(\boldsymbol{\alpha}, \mathbf{p})^2) \quad (12)$$

$$\mathbf{a}^l = \text{Argmin}_{\mathbf{a}^l} (\chi_u(\boldsymbol{\alpha}, \mathbf{p})^2) \quad (13)$$

i.e., minimization of χ_u^2 with respect to the additional mode is considered.

A general overview of the 4D PGD P-DVC procedure is shown in the algorithm 1. Even though a maximum value of iterations or convergence criteria ϵ_p , and ϵ_α can be enforced to stop the fixed-point algorithm, this revealed unnecessary as the maximum number of iterations to reach stagnation is usually quite low (*i.e.*, 3-5).

Algorithm 1 General 4D-P-DVC fixed-point procedure

while High residual norm **do**

 Initialize \mathbf{a}^l and \mathbf{p}^l

 Correction $f(\mathbf{x}) \leftarrow f(\mathbf{x} - \mathbf{u}^{l-1})$

while $\|\Delta \Phi_i\| < \epsilon_p$ and $\|\Delta \boldsymbol{\alpha}^l\| < \epsilon_\alpha$ **do**

 Compute spatial mode \mathbf{p}^l , Equation 14

 Compute temporal amplitude \mathbf{a}^l , Equation 17

end while

 Update displacement field \mathbf{u}^l , Equation 11 $l = l + 1$

end while

The two parts of the fixed point algorithm are obtained from the above linearized functional using Newton's scheme. The derivative with respect to \mathbf{p} leads to

$$\mathbf{p}^l = \mathbf{N}^{-1}\mathbf{n} \quad (14)$$

with \mathbf{N} the spatial Hessian matrix of $\chi_{\mathbf{u}}^2$ with respect to \mathbf{p} (*i.e.*, $N_{ij} = \partial_{p_i}\partial_{p_j}\chi_{\mathbf{u}}^2$) and \mathbf{n} the second member vector based on the residual field

$$N_{ij} = \sum_{k,\mathbf{r}} \alpha^l(\theta_k)^2 \Pi_k[\boldsymbol{\psi}_i(\mathbf{x}') \cdot \nabla f(\mathbf{x}')] \Pi_k[\boldsymbol{\psi}_j(\mathbf{x}') \cdot \nabla f(\mathbf{x}')] \quad (15)$$

and

$$n_i = \sum_{k,\mathbf{r}} \alpha^l(\theta_k) (s(\mathbf{r}, \theta_k) - \Pi_k[f(\mathbf{x}')]) \Pi_k[\boldsymbol{\psi}_i(\mathbf{x}') \cdot \nabla f(\mathbf{x}')] \quad (16)$$

where \mathbf{x}' is the advected position of the volume with the previously identified modes such that $\mathbf{x}' = \mathbf{x} - \mathbf{u}^{l-1}$.

Similarly, the derivative with respect to \mathbf{a}^l leads to

$$\mathbf{a}^l = \mathbf{M}^{-1}\mathbf{m} \quad (17)$$

where, as previously, \mathbf{M} is the temporal Hessian matrix (*i.e.*, $M_{ij} = \partial_{a_i}\partial_{a_j}\chi_{\mathbf{u}}^2$) and \mathbf{m} the second member vector based on the residual field

$$M_{ij} = \sum_{k,\mathbf{r}} \sigma_i(\theta_k) \Pi_k[\boldsymbol{\Phi}^l(\mathbf{x}') \cdot \nabla f(\mathbf{x}')] \sigma_j(\theta_k) \Pi_k[\boldsymbol{\Phi}^l(\mathbf{x}') \cdot \nabla f(\mathbf{x}')] \quad (18)$$

and

$$m_j = \sum_{k,\mathbf{r}} (s(\mathbf{r}, \theta_k) - \Pi_k[f(\mathbf{x}')]) \sigma_j(\theta_k) \Pi_k[\boldsymbol{\Phi}^l(\mathbf{x}') \cdot \nabla f(\mathbf{x}')] \quad (19)$$

The residual field at convergence, $\rho(\mathbf{r}, \theta_k) \equiv (s(\mathbf{r}, \theta_k) - \Pi_k[f(\mathbf{x}'))$ for the N_θ 2D projections, gives a very precious information on the quality of the solution in the projected domain, which is parameterized by \mathbf{r} . Its norm is the minimized quantity and defines the convergence criterion. Ideally, it consists of acquisition noise and artifacts. It is thus a natural place to judge whether some spurious displacement is to be corrected for.

2.4. Comparison metric

In order to show the improvement provided by the method, comparisons at 2 steps are performed. The first one is the measurement of the norm of the residual between the projections of the final reconstructed volume and the acquired radiographs. This norm is the minimized quantity of interest hence this is the true metric of the present procedure. The Signal to Noise Ratio (SNR) can also be defined to evaluate the residual quantitatively. The higher the SNR, the better the solution. It is defined as 20 times the decimal logarithm of the ratio of the standard deviation of the projections $\sigma(s)$ over that of the residual fields $\sigma(\rho)$

$$SNR(t) = 20 \log_{10} \left(\frac{\sigma(s)}{\sigma(\rho)} \right) \quad (20)$$

One may also be interested in the quality of the reconstructed volume itself. A visual estimation of the sharpness of the image can be supported by the value of the Shannon information entropy that has to be minimized,

$$S = - \sum_f p(f) \log_{10}[p(f)] \quad (21)$$

where $p(f)$ is the gray level distribution (*i.e.*, probability of observing a gray level equal to f).

3. Application

3.1. Test case

The application case where the set of radiographs has been extracted is an *in situ* tensile test on a cast iron sample. The sample (Figure 1(a)), which was mounted in an *in situ* testing machine similar to that used by Buffière *et al* [47], was scanned at LMT lab-tomograph (X-View X50-CT, North Star Imaging, 129 kV, 95 μ A, W target). The voxel size at full resolution was set to 2.8 μ m. The complete scan of the reference state consists of 1,000 radiographs captured at equally spaced angles ranging over a full 360° revolution. Two flat-fields are acquired after conditioning and before the experiment in order to perform flat-field corrections. One dark-field has also been acquired before the experiment. Each radiograph is averaged over 30 frames in order to reduce acquisition noise. The acquired radiographs have a definition of 1944 \times 1536 pixels² but the following procedure deals with two lower scales. Coarse graining into superpixels of size 2 \times 2 (and 4 \times 4) is carried out with the convolution of the images by a Gaussian kernel with a characteristic width of 2 (and 4) pixels. The resulting image is downsampled over a coarse 2 \times 2 (resp. 4 \times 4) regular square grid to create smaller images (called image at scale 2 and scale 4). The projections are obtained after flat field normalization and standard beam hardening correction [48] due to the high absorption of the cast iron with a third order polynomial.

Reconstructions and projections are performed with ASTRA toolbox [49]. It is obtained with Feldkamp-Davis-Kress (FDK) procedure suited for cone beams [6]. The geometric parameters for the initialization are given by the offline (*i.e.*, standard) calibration of the tomograph that uses a pattern composed of vertical calibrated steel balls. This offline procedure is very fast (*i.e.*, approximately one minute) and has been performed once at the beginning of the experiment. It can be noted that this initialization is not needed and could be replaced by the use of the proposed approach only.

The entire test of 16 loading steps has been performed over few days because each acquisition requires about 2 h. The acquired projections and the reconstructed volume are shown in Figure 1(a,b). Because of cone beam artifacts at the top and bottom of reconstructions, the projected ROI definition is $90 < z < 897$ pixels for scale 2, and $45 < z < 449$ pixels for scale 4.

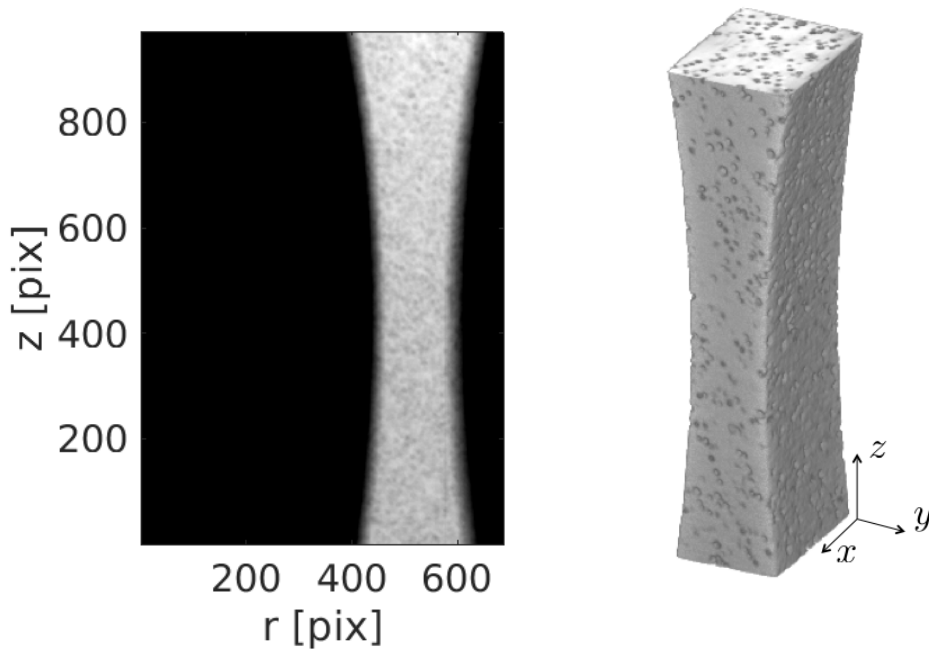


Figure 1. (a) Acquired projections for $\theta = 0^\circ$. (b) Corresponding reconstruction

Overnight, the grip displacements are held at a fixed value and nothing is supposed to move. In spite of this assumption, a DVC analysis of the test shows large motion and residuals between two scans separated by one night, which will be called steps 1 and 2. Because of the presence of the testing machine, the standard calibration procedure based on the rotation of a known target (made of steel balls) is impossible during the *in situ* process. A reconstruction of these two steps with ASTRA shows a very large change on the reconstruction parameters. The reconstruction at step 1 gives a very good (*i.e.*, sharp) result. With the very same parameters, scan 2, which was acquired the day after, is poorly reconstructed. Slices of the reconstructions of step 1 and 2 in Figures 2 and 3 show the effect of overnight parameter variations. The Shannon entropy of the two volumes is 5.93 and 6.12, respectively for steps 1 and 2. This marked increase corresponds to drift of geometrical parameters.

The proposed application procedure deals with the two scans in order to find the correct geometric parameters. The two previous identification methods are used. The first test case, in Section 3.2, is step 2 at scale 4. For this calibration the correction is large hence it may require many displacement modes. However because the total number of degrees of freedom is small (*i.e.*, 6 RBMs \times 4 time functions), a full measurement is performed. The second application, in Section 3.3, is the correction of step 1 at scale 2. Because the displacement level is not very high, the kinematics is captured with the modal decomposition constrained by time functions. It is shown that three modes are sufficient to capture almost all the kinematics. Instead of working with the 1,000 radiographs, for computation cost and because no high frequency displacement is expected, a subset of 100 regularly spaced radiographs is used.

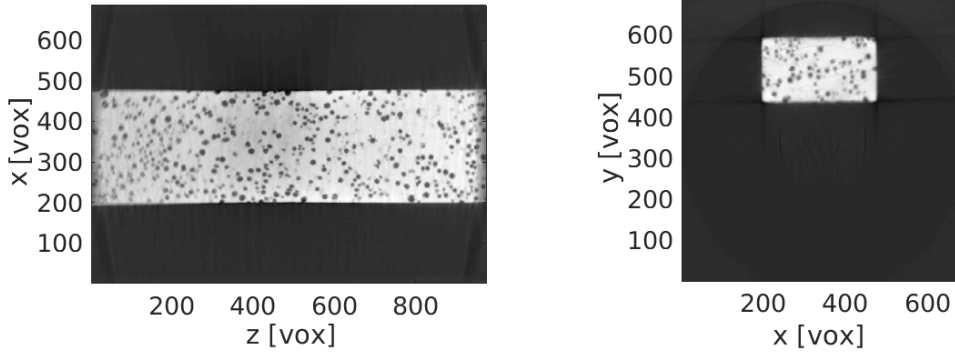


Figure 2. Slices of the reconstruction of step 1 for (left) $y = 500$ voxels and (right) $z = 150$ voxels. The top and bottom parts are slightly blurred due to motion or tilted rotation axis

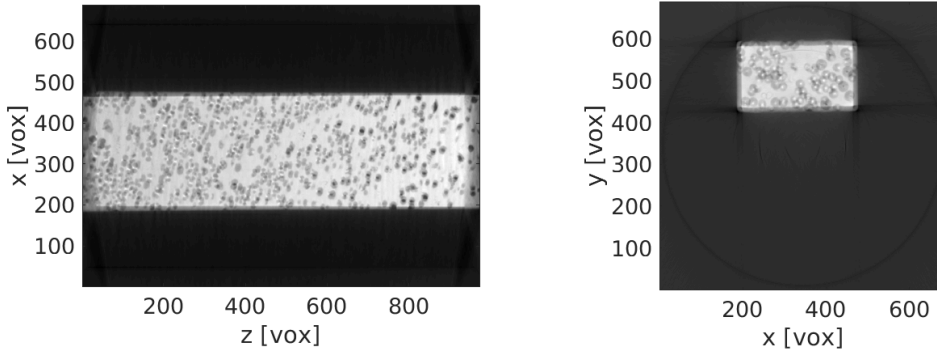


Figure 3. Slices of the reconstruction of step 2 for (left) $y=500$ voxels and (right) $z=150$ voxels. The top and bottom parts are severely blurred due to motion or tilted rotation axis

As previously discussed, the amplitude vector \mathbf{a} can be scaled by an arbitrary factor if \mathbf{p} is scaled by its inverse. To make the results comparable and easily understandable, this scale factor was chosen so that $\alpha(\theta_k)$ varies within the interval $[-1, 1]$. The associated space mode amplitude thus corresponds to the maximum displacement amplitude.

3.2. Full identification

The first test case is step 2. Overnight, the geometric parameters changed. Because large motions are anticipated, the analysis is performed at scale 4 and a full identification (*i.e.*, determination of all space and time degrees of freedom, as earlier defined) is performed. The space regularization used in the modal measurement approach is composed of the six RBMs, and the temporal shape functions consist of sine and cosine functions with a period of 2π , a constant offset and a linear change. The sine and cosine functions are suited to model for example a steady rotation axis in the lab frame. The linear

component captures the kinematics of non-periodic motions such as sample motions. Thus, the kinematic basis is composed of 24 degrees of freedom (*i.e.*, 6 RBMs \times 4 time functions).

The initial and final residuals are shown in Figure 4. The mean SNR increases from 20.3 to 28.5. This huge enhancement means that a very large part of the actual kinematics is captured. The residuals on the edges of the sample are not totally corrected but may come from the blurred volume itself.

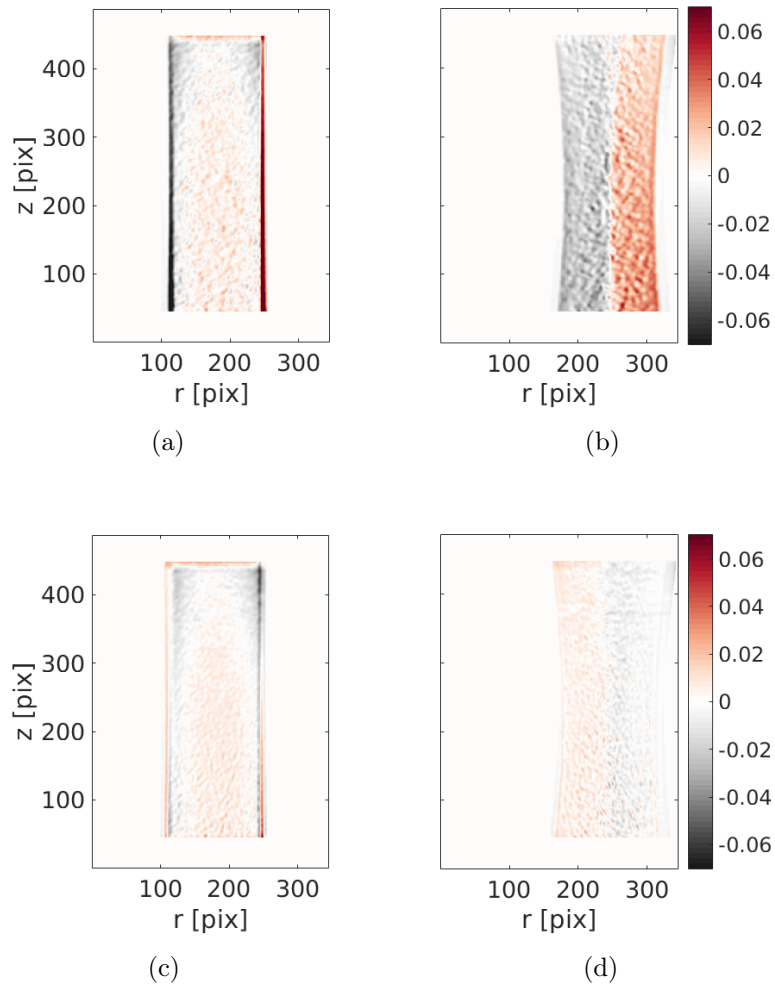


Figure 4. Initial and final residual fields after the correction of the three modes when (a) $\theta_k = 90^\circ$ and (b) $\theta_k = 330^\circ$

The angular SNR before and after displacement field correction is shown in Figure 5. It is measured on a smaller scale thus its level is not really comparable with the previous values.

The axis of rotation is extracted from the displacement field. It is plotted in Figure 6 with the previously identified axis at step 1. It can be seen that the displacement is composed of a large translation (*i.e.*, radius of 3.9 voxels) and a rotation that is similar

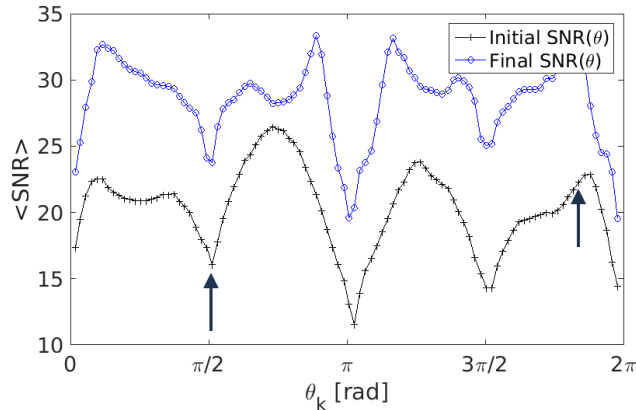


Figure 5. Initial and final angular SNRs for step 2 with the full measurement approach. The two arrows show the position of the extracted residuals of Figure 4

to the previous identification. The displacement consists of an important motion along the X direction because the procedure is not very sensitive to motions in the direction of the X-ray beam (*i.e.*, the X direction of the laboratory frame is that of the central axis of the cone beam).

The corrected volume shows huge improvements in terms of visual quality (Figure 7) with sharp nodules and edges. The Shannon entropy (initially at 6.12) decreases to 5.79.

3.3. Modal measurement

3.3.1. Initial residual fields and regularization The second test case is step 1. Because small motions are expected, the analysis is performed with a modal measurement at scale 2. The initial residual fields are shown in Figure 8. In these fields, the top and bottom parts are composed of high values due to cone beam reconstruction and projection artifacts. These areas are not taken into account in the identification procedure and are masked. The residual field is made of positive and negative patterns, which is a signature of displacements, and more precisely, a rotation on the top and bottom parts. The mean SNR level is 24.5.

3.3.2. Displacement mode identification The identification is composed of three space-time modes. The mean SNR after the correction of each mode is shown in Table 1. Three modes are sufficient to capture the kinematics because the SNR does not increase much after mode 3.

Table 1. Mean SNR as a function of the number of correction modes. A fast convergence with three modes is noted

Mode l	0	1	2	3	4
$\langle \text{SNR} \rangle_l$	24.5	25.8	26.7	26.8	26.8

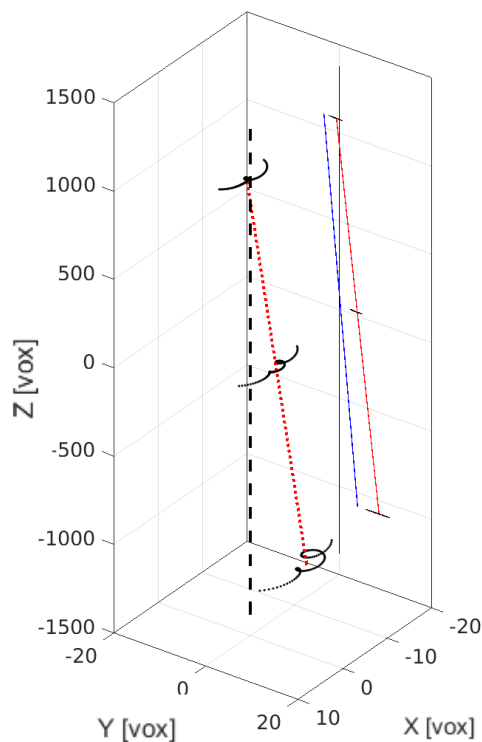


Figure 6. Mean displacements of the top, center and bottom parts of the sample in the laboratory frame and their projections in the detector frame. The projected blue line is the next identified rotation axis for the first step in the next section

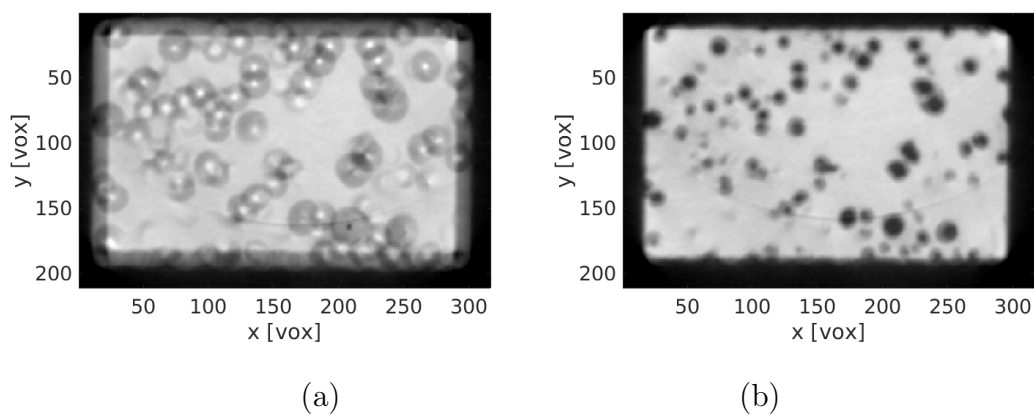


Figure 7. Zoom on the reconstruction of step 2 at slice $z = 100$ voxels (a) for the initial state and (b) after correction of the rotation axis

The angular SNR is shown in Figure 9. Low SNRs at every $\pi/2$ increment (*i.e.*, alignment of the sample edges with the beam direction) are interpreted as phase contrast. It is worth noting that the first two modes are complementary and affect different angular

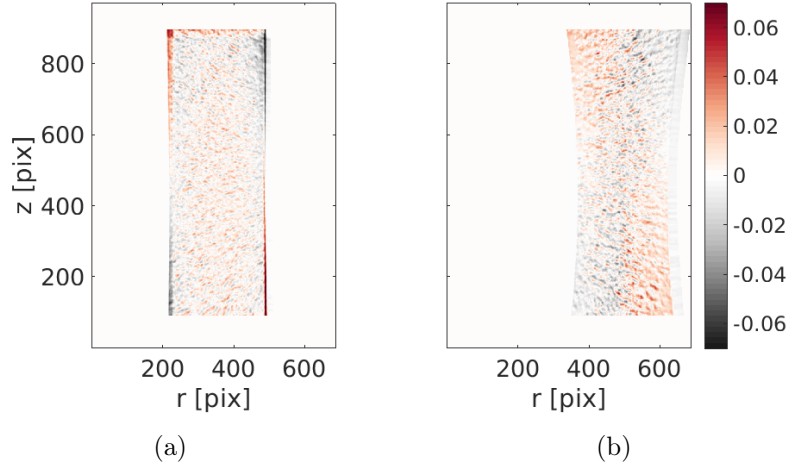


Figure 8. Initial residual fields when (a) $\theta_k = 90^\circ$ and (b) $\theta_k = 330^\circ$ with the same color bar. A high positive and negative residual is the signature of motion

sectors.

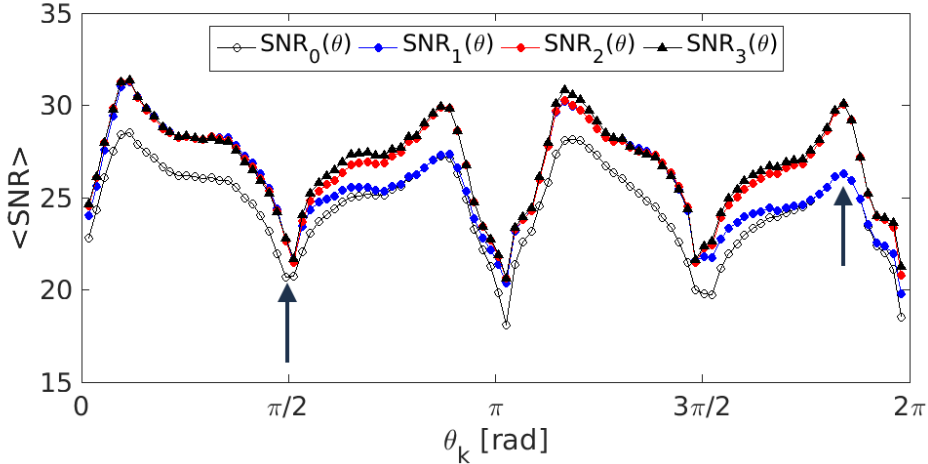


Figure 9. SNR(θ) for all treated angles after successive additions of modes. The two arrows show the position of the extracted residuals of Figure 10

The final residual fields after corrections with the measured displacement field are shown in Figure 10. The residual is much smoother and a part of the rotation motion has been corrected.

The space and time functions of the three modes are shown in Figures 11, 12 and 13. The spatial mode is shown on a mesh of the sample and expressed in voxels. The scanned part of this mesh is the curved zone in the center. The top and bottom parts are outside of the projections and correspond to the entire tested specimen.

In order to validate the choice of the time basis, the result of the mode identification with Dirac time functions (*i.e.*, with no temporal regularization) is shown in the same

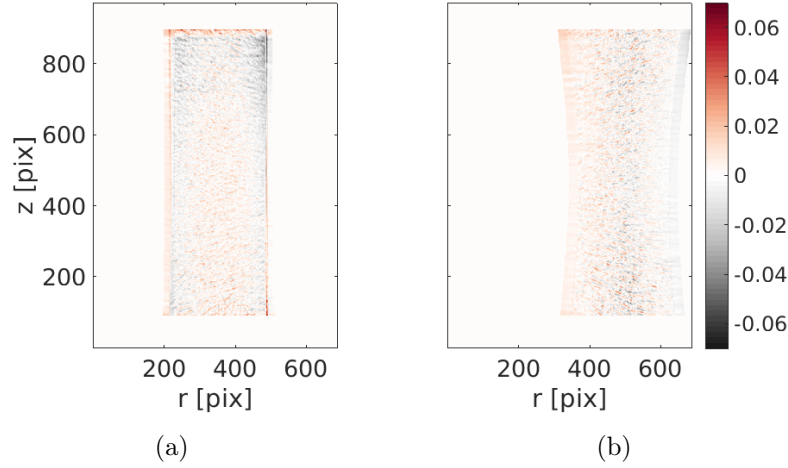


Figure 10. Final residual fields after the correction with three modes for (a) $\theta_k = 90^\circ$ and (b) $\theta_k = 330^\circ$

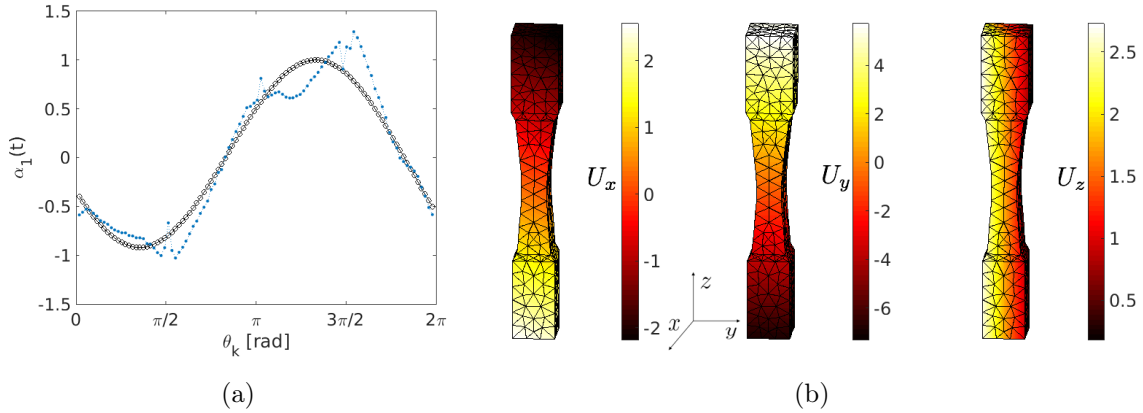


Figure 11. First mode. (a) Temporal mode with (black circles) and without (blue points) time constraints. (b) Spatial mode in the x, y, z directions, expressed in voxels on the mesh (1 voxel \equiv $5.6 \mu\text{m}$)

plot. This temporal measurement is performed with the same spatial modes (it can be noted that in the case of a purely free identification, the results would have been different because of different spatial modes). It is observed that, for the first two modes, the free and constrained temporal histories are close to each other. Hence the chosen time functions provide an appropriate basis. For mode 3, the vertical component of the displacement field is close to zero, so that the sensitivity is low for some projection angles. The difference of time history between the free and constrained functions is on these non-sensitive projection angles (*i.e.*, $\pi/2$ and $3\pi/2$). For those angles, the time regularization is important to correctly capture the kinematics. Because these angles lack sensitivity, they bear very little weights in the procedure (see Figure 13) and the regularized time function is not a mere least squares fit of the free form but is weighted by sensitivities. These results also show the benefit of reducing the number of temporal

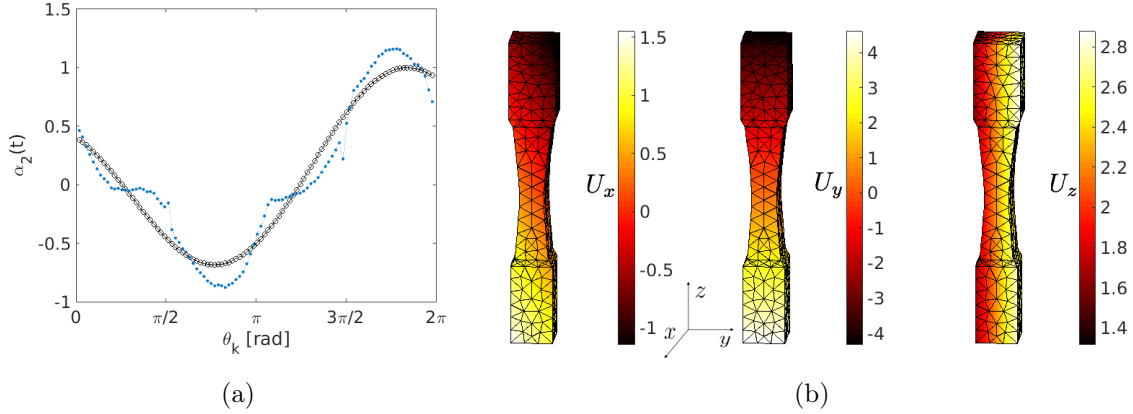


Figure 12. Second mode. (a) Temporal mode with (black circles) and without (blue points) time constraints. (b) Spatial mode in the x, y, z directions, expressed in voxels on the mesh (1 voxel \equiv $5.6 \mu\text{m}$)

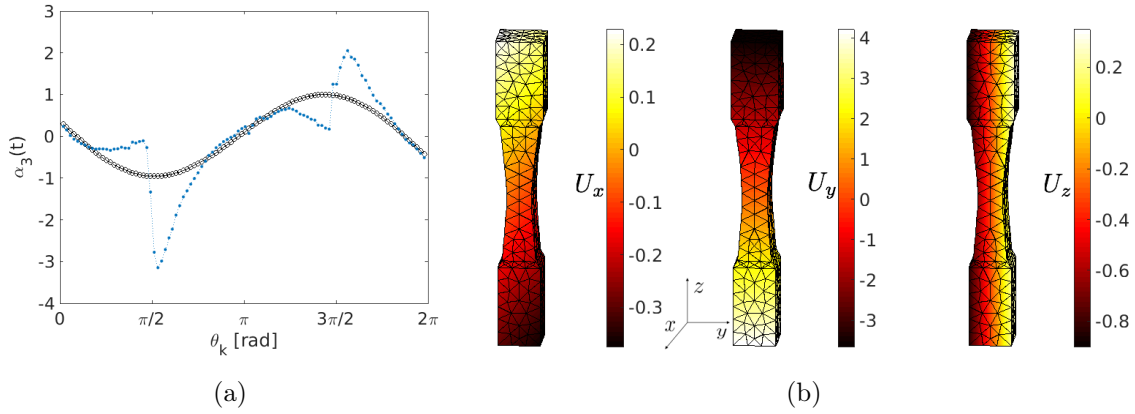


Figure 13. Third mode. (a) Temporal mode with (black circles) and without (blue points) time constraints. (b) Spatial mode in the x, y, z directions, expressed in voxels on the mesh (1 voxel \equiv $5.6 \mu\text{m}$). The difference between the free and constrained time history is due to a lack of sensitivity on the displacement field at angles $\pi/2$ and $3\pi/2$

modes so that the conditioning of the system is enhanced and physically realistic modes are extracted.

3.3.3. Correction and reconstruction The 3D displacement of the volume gives access to the position of the real rotation axis. Because it is defined in a basis linked to the rotating sample, the motion has to be projected to the laboratory frame. The mean projected displacements of the top, center and bottom parts of the sample are shown in Figure 14. The red line is the mean position of the sample axis during rotation.

The volume can now be corrected with the projection motions. Hence a new set of projections is obtained and the reconstructed volume is updated accordingly. Figure 15 shows the corrected reconstruction. The information entropy for this corrected volume is 5.74 (to be compared to the initial value of 5.93), meaning that the edges and

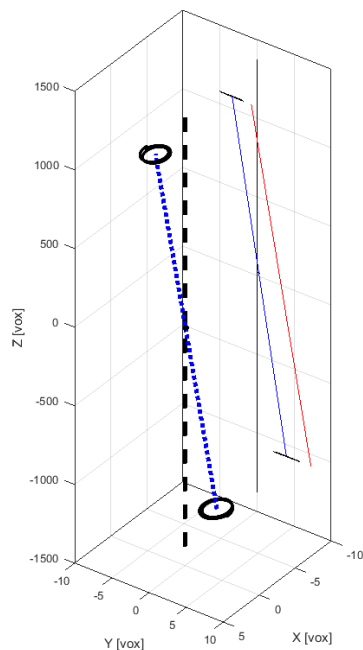


Figure 14. Mean displacement of the top, center and bottom parts of the sample in the laboratory frame and its projection on the detector frame. The axis of the X-ray cone beam is X

microstructural details are sharper. After this step, a new correction iteration can be performed. However, because the displacement magnitude is small, most of the kinematics was captured in this first step.

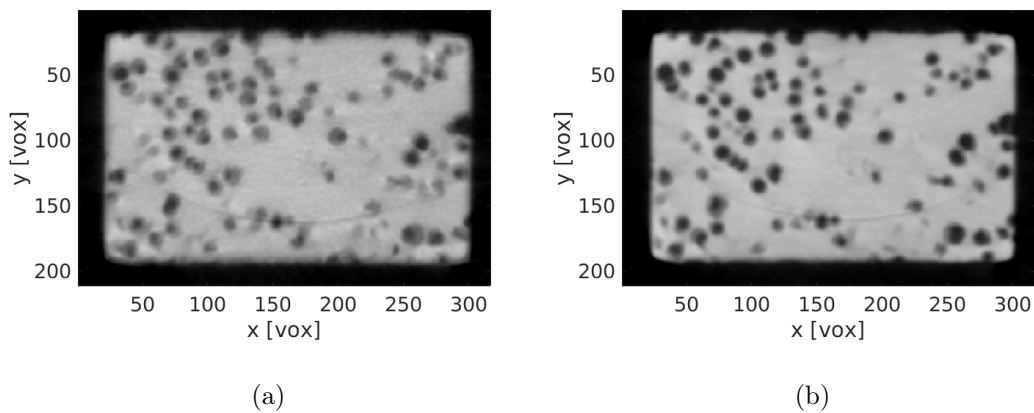


Figure 15. Zoom on the reconstruction of step 1 for slice $z = 100$ voxels (a) for the initial state, (b) after correction of the rotation axis

4. Conclusion

An online calibration procedure for cone beam X-ray tomography based on projection-based Digital Volume Correlation has been proposed. This technique, which does not require any change from the standard acquisition protocol, repositions an initially reconstructed volume in a given 3D frame so that each of its projection matches, for each angle, the initial sinogram. The position is given by a displacement field decomposed over space (*i.e.*, rigid body motions) and time (*i.e.*, angular) basis functions. The identified position of the volume over time reveals the instantaneous rotation axis while scanning the sample and the drift of the set-up.

In order to preserve a good conditioning of the system, a model reduction technique based on Proper Generalized Decomposition is introduced so that key modes are progressively added to reduce the projection residuals.

The two application tests, which are extracted from a 4D mechanical test, with two different calibration procedures show very significant improvements in the reconstruction quality and much lower residual fields, thereby proving that the corrections account for most of the initial inconsistencies. With much less reconstruction artifacts, the updated volumes can be further used for quantitative kinematic measurements. In addition to the norm of the residual fields, Shannon entropy is used to assess the calibration improvement on the updated volume.

The method works with small displacements compared to the microstructure length and yields sub-pixel uncertainties. In cases of larger displacements, the 3D volume can first be updated with a coarse initialization (*e.g.*, obtained from previous computations, multi-scale procedures or cross-correlations). An update of the procedure with the corrected reconstruction could reveal necessary if the displacement is not well captured at the first iteration.

An additional improvement of the present procedure would be to use algebraic reconstruction methods for which the metric is already an L2-norm between the re-projected reconstructed volume and the available projections.

In the presented test cases, a simple spatial regularization composed of rigid body motions is used (and is sufficient) to reposition the volume. However, the method is not limited to such cases. For instance when analyzing mechanical tests with continuous loading [5], the spatial regularization could be complemented with other elementary modes including deformations (*e.g.*, tension or compression). This could also be performed to account for viscoelasticity or viscoplasticity during the scan.

Coupled with fast acquisition devices and applied to the measurement of displacement fields during continuously loaded mechanical tests, this method could give access to ultra-fast mechanical identification that could not be performed with classical means such as 3D or 4D DVC.

5. Acknowledgement

This work has benefited from the support of the French “Agence Nationale de la Recherche”, through the “Investissements d’avenir” Program MATMECA (ANR-10-EQPX-37 grant), and the COMINSIDE project (ANR-14-CE07-0034-02 grant). The authors would like to acknowledge Dr. Matthieu Vitse for precious advices on PGD methods.

References

- [1] J. Baruchel, J.Y. Buffière, E. Maire, P. Merle, and G. Peix, editors. *X-Ray Tomography in Material Sciences*. Hermès Science, Paris (France), 2000.
- [2] J. Desrues, G. Viggiani, and P. Bésuelle, editors. *Advances in X-ray Tomography for Geomaterials*. Wiley / ISTE, London (UK), 2006.
- [3] A.C. Kak and M. Slaney. *Principles of computerized tomographic imaging*. IEEE press, 1988.
- [4] L. Salvo, M. Suéry, A. Marmottant, N. Limodin, and D. Bernard. 3D imaging in material science: Application of X-ray tomography. *Comptes Rendus Physique*, 11(9):641–649, 2010.
- [5] E. Maire, C. Le Bourlot, J. Adrien, A. Mortensen, and R. Mokso. 20 Hz X-ray tomography during an in situ tensile test. *International Journal of Fracture*, 200(1):3–12, 2016.
- [6] L.A. Feldkamp, L.C. Davis, and J.W. Kress. Practical cone-beam algorithm. *JOSA A*, 1(6):612–619, 1984.
- [7] F. Hild, A. Bouterf, L. Chamoin, H. Leclerc, F. Mathieu, J. Neggers, F. Pled, Z. Tomičević, and S. Roux. Toward 4D Mechanical Correlation. *Advanced Modeling and Simulation in Engineering Sciences*, 3(1):17, 2016.
- [8] M. Ferrucci, R. K Leach, C. Giusca, S. Carmignato, and W. Dewulf. Towards geometrical calibration of x-ray computed tomography systems—a review. *Measurement Science and Technology*, 26(9):092003, 2015.
- [9] Y. Cho, D.J. Moseley, J.H. Siewerdsen, and D.A. Jaffray. Accurate technique for complete geometric calibration of cone-beam computed tomography systems. *Medical physics*, 32(4):968–983, 2005.
- [10] K. Yang, A.L.C. Kwan, D.F. Miller, and J.M. Boone. A geometric calibration method for cone beam CT systems. *Medical physics*, 33(6):1695–1706, 2006.
- [11] J. Baek, B. De Man, J. Uribe, R. Longtin, D. Harrison, J. Reynolds, B. Neele, K. Frutsky, L. Inzinna, A. Caiafa, et al. A multi-source inverse-geometry CT system: initial results with an 8 spot x-ray source array. *Physics in medicine and biology*, 59(5):1189, 2014.
- [12] S. Carmignato, A. Pierobon, P. Rampazzo, M. Parisatto, and E. Savio. CT for industrial metrology-accuracy and structural resolution of CT dimensional measurements. Conference on Industrial Computed Tomography (ICT), 2012.
- [13] Y. Sun, Y. Hou, F. Zhao, and J. Hu. A calibration method for misaligned scanner geometry in cone-beam computed tomography. *NDT & E International*, 39(6):499–513, 2006.
- [14] J. Zhao, X. Hu, J. Zou, and X. Hu. Geometric parameters estimation and calibration in cone-beam micro-CT. *Sensors*, 15(9):22811–22825, 2015.
- [15] Q. Xiang, J. Wang, and Y. Cai. A geometric calibration method for cone beam CT system. In *Eighth International Conference on Digital Image Processing (ICDIP 2016)*, pages 100333G–100333G. International Society for Optics and Photonics, 2016.
- [16] N. Limodin, J. Réthoré, J. Adrien, J.Y. Buffière, F. Hild, and S. Roux. Analysis and artifact correction for volume correlation measurements using tomographic images from a laboratory X-ray source. *Exp. Mech.*, 51(6):959–970, 2011.
- [17] J. Lemaitre and J.L. Chaboche. *Mechanics of Solid Materials*. Cambridge University Press, Cambridge (UK), 1990.

- [18] E.C.G. Andò. *Étude expérimentale de l'évolution de la microstructure d'un milieu granulaire sous chargement mécanique à l'aide de tomographie à rayons-x*. PhD thesis, Université de Grenoble, 2013.
- [19] D. Panetta, N. Belcari, A. Del Guerra, and S. Moehrs. An optimization-based method for geometrical calibration in cone-beam CT without dedicated phantoms. *Physics in Medicine and Biology*, 53(14):3841, 2008.
- [20] Y. Kyriakou, R.M. Lapp, L. Hillebrand, D. Ertel, and W.A. Kalender. Simultaneous misalignment correction for approximate circular cone-beam computed tomography. *Physics in Medicine and Biology*, 53(22):6267, 2008.
- [21] Y. Otake, S. Schafer, J.W. Stayman, W. Zbijewski, G. Kleinszig, R. Graumann, A.J. Khanna, and J.H. Siewerdsen. Automatic localization of vertebral levels in x-ray fluoroscopy using 3D-2D registration: a tool to reduce wrong-site surgery. *Physics in medicine and biology*, 57(17):5485, 2012.
- [22] Y. Otake, A.S. Wang, J.W. Stayman, A. Uneri, G. Kleinszig, S. Vogt, A.J. Khanna, Z.L. Gokaslan, and J.H. Siewerdsen. Robust 3D-2D image registration: application to spine interventions and vertebral labeling in the presence of anatomical deformation. *Physics in medicine and biology*, 58(23):8535, 2013.
- [23] S. Ouadah, J.W. Stayman, G.J. Gang, T. Ehtiati, and J.H. Siewerdsen. Self-calibration of cone-beam CT geometry using 3D-2D image registration. *Physics in medicine and biology*, 61(7):2613, 2016.
- [24] J. Kim, J. Nuyts, A. Kyme, Z. Kuncic, and R. Fulton. A rigid motion correction method for helical computed tomography (CT). *Physics in medicine and biology*, 60(5):2047, 2015.
- [25] T. Sun, J.H. Kim, R. Fulton, and J. Nuyts. An iterative projection-based motion estimation and compensation scheme for head x-ray CT. *Medical Physics*, 43(10):5705-5716, 2016.
- [26] M.A. Sutton. Computer Vision-Based, Noncontacting Deformation Measurements in Mechanics: A Generational Transformation. *Appl. Mech. Rev.*, 65(AMR-13-1009):050802, 2013.
- [27] B.K. Bay, T.S. Smith, D.P. Fyhrie, and M. Saad. Digital volume correlation: three-dimensional strain mapping using X-ray tomography. *Experimental mechanics*, 39(3):217-226, 1999.
- [28] T.S. Smith, B.K. Bay, and M.M. Rashid. Digital volume correlation including rotational degrees of freedom during minimization. *Experimental Mechanics*, 42(3):272-278, 2002.
- [29] H. Leclerc, S. Roux, and F. Hild. Projection savings in CT-based digital volume correlation. *Experimental Mechanics*, 55(1):275-287, 2015.
- [30] T. Taillandier-Thomas, C. Jailin, S. Roux, and F. Hild. Measurement of 3D displacement fields from few tomographic projections. In *SPIE Photonics Europe*, page 98960. International Society for Optics and Photonics, 2016.
- [31] T. Taillandier-Thomas, S. Roux, and F. Hild. A soft route toward 4D tomography. *Physical Review Letters*, 117(2):025501, 2016.
- [32] C. Jailin, A. Bouterf, M. Poncelet, and S. Roux. In situ μ CT-scan mechanical tests: Fast 4D mechanical identification. *Experimental Mechanics*, Accepted, 2017.
- [33] S. Roux, F. Hild, P. Viot, and D. Bernard. Three-dimensional image correlation from X-ray computed tomography of solid foam. *Composites Part A: Applied science and manufacturing*, 39(8):1253-1265, 2008.
- [34] J. Réthoré, S. Roux, and F. Hild. An extended and integrated digital image correlation technique applied to the analysis of fractured samples: The equilibrium gap method as a mechanical filter. *European Journal of Computational Mechanics/Revue Européenne de Mécanique Numérique*, 18(3-4):285-306, 2009.
- [35] Z. Tomicevic, F. Hild, and S. Roux. Mechanics-Aided Digital Image Correlation. *J. Strain Analysis*, 48:330-343, 2013.
- [36] H. Leclerc, J.-N. Périé, S. Roux, and F. Hild. Voxel-scale digital volume correlation. *Experimental Mechanics*, 51(4):479-490, 2011.
- [37] T. Taillandier-Thomas, S. Roux, T.F. Morgeneyer, and F. Hild. Localized strain field measurement

- on laminography data with mechanical regularization. *Nuclear Instruments and Methods in Physics Research Section B: Beam Interactions with Materials and Atoms*, 324:70–79, 2014.
- [38] A. Bouterf, S. Roux, F. Hild, J. Adrien, E. Maire, and S. Meille. Digital Volume Correlation Applied to X-ray Tomography Images from Spherical Indentation Tests on Lightweight Gypsum. *Strain*, 50(5):444–453, 2014.
- [39] G. Besnard, S. Guérard, S. Roux, and F. Hild. A space–time approach in digital image correlation: Movie-DIC. *Optics and Lasers in Engineering*, 49(1):71–81, 2011.
- [40] G. Besnard, H. Leclerc, S. Roux, and F. Hild. Analysis of Image Series through Digital Image Correlation. *J. Strain Analysis*, 47(4):214–228, 2012.
- [41] A. Nouy. A priori model reduction through proper generalized decomposition for solving time-dependent partial differential equations. *Computer Methods in Applied Mechanics and Engineering*, 199(23):1603–1626, 2010.
- [42] P. Ladevèze. *Nonlinear computational structural mechanics: new approaches and non-incremental methods of calculation*. Springer Science & Business Media, 2012.
- [43] M. Vitse. *Model-order reduction for the parametric analysis of damage in reinforced concrete structures*. PhD thesis, Université Paris-Saclay, 2016.
- [44] J.C. Passieux and J.N. Périé. High resolution digital image correlation using proper generalized decomposition: PGD-DIC. *International Journal for Numerical Methods in Engineering*, 92(6):531–550, 2012.
- [45] L.A. Gomes Perini, J.C. Passieux, and J.N. Périé. A Multigrid PGD-based Algorithm for Volumetric Displacement Fields Measurements. *Strain*, 50(4):355–367, 2014.
- [46] T.H. Cormen. *Introduction to algorithms*. MIT press, 3rd edition, 2009.
- [47] J.-Y. Buffiere, E. Maire, J. Adrien, J.-P. Masse, and E. Boller. In situ experiments with X ray tomography: an attractive tool for experimental mechanics. *Experimental mechanics*, 50(3):289–305, 2010.
- [48] G.T. Herman. Correction for beam hardening in computed tomography. *Physics in medicine and biology*, 24(1):81, 1979.
- [49] W. Van Aarle, W.J. Palenstijn, J. De Beenhouwer, T. Altantzis, S. Bals, K.J. Batenburg, and J. Sijbers. The ASTRA Toolbox: A platform for advanced algorithm development in electron tomography. *Ultramicroscopy*, 157:35–47, 2015.